Misfit-layered cobaltite with an anisotropic giant magnetoresistance: $Ca_3Co_4O_9$

A. C. Masset, C. Michel,* A. Maignan, M. Hervieu, O. Toulemonde, F. Studer, and B. Raveau
Laboratoire CRISMAT, UMR 6508 associée au CNRS, ISMRA et Université de Caen 6, Boulevard du Maréchal Juin, 14050 CAEN Cedex, France

J. Hejtmanek
Laboratory of Oxidic Materials, Institute of Physics, 162 53 Prague 6, Cukrovarnicka 10, Czech Republic
(Received 1 February 2000)

Combining electron diffraction, x-ray diffraction, and high-resolution electron microscopy techniques, a structural model for the cobaltite ''$Ca_3Co_4O_9$'' has been found. This compound is a misfit-layered oxide consisting in two monoclinic subsystems with identical *a*, *c*, and β parameters, but different *b* parameters: $a=4.8376(7)$ Å, $c=10.833(1)$ Å, $\beta=98.06(1)°$, $b_1=4.5565(6)$ Å, and $b_2=2.8189(4)$ Å. The structure is built up from the stacking along *c* of triple rock salt-type layers Ca_2CoO_3 (first subsystem) with single CdI_2-type CoO_2 layers (second subsystem). Two different sets of Co-O distances are involved which are interpreted as the existence of cobalt with three different oxidation states 2+, 3+, and 4+, in agreement with x-ray appearance near-edge structure spectra at the Co *K* edge. At about 420 K, both resistivity and susceptibility show an anomaly which results from a spin-state transition of cobalt at this temperature. Below 300 K, the resistivity measured along the CoO_2 layers shows a metal-insulator transition as *T* decreases, whereas the much larger out-of-plane resistivity values show the anisotropic behavior of this phase. The application of a magnetic field induces a negative magnetoresistance which reaches −35% for 7 T. Moreover, thermoelectric power measurements yield a high positive value of $\approx 125\ \mu V\,K^{-1}$ at 300 K with a weak temperature dependence in between 100 and 300 K. This result contrasts with the metallic in-plane resistivity.

I. INTRODUCTION

A series of thallium and bismuth cobaltites, $Tl_\alpha[(Sr, Ca)_{1-\beta}O]_{1+x}CoO_2$,[1,2]

$$Bi_\alpha[A_{0.75}Bi_{0.25}O]_{(3+3x)/2}CoO_2 \quad (A=Ca, Sr),$$[3]

and $[Bi_{0.82}SrO_2]_2[CoO_2]_{1.82}$,[4,5] has recently been synthesized. These compounds represent the first oxides with a misfit-layered structure similar to that observed previously for chalcogenides.[6–8] Their structure consists of single $[CoO_2]$ layers of the CdI_2 type, stacked with SrO (or CaO) and BiO rocksalt-type layers. The discordance between the sublattices of these two types of layers makes it such that such composite crystals are expected to exhibit strongly anisotropic properties.

From the viewpoint of magnetoresistance properties, cobalt oxides are potential materials, as shown for the tridimensional perovskite $La_{1-x}Sr_xCoO_3$ (Refs. 9–11) and for the bidimensional cobaltites $Bi_{0.5}Cd_{0.3}Sr_2Co_{1.2}O_5$ (Ref. 12) and $LnBaCo_2O_{5+\delta}$ (Ref. 13), for which giant magnetoresistance (GMR) properties have been evidenced. In contrast to the latter, the Tl- or Bi-based misfit-layered cobaltites do not show any GMR effect. Moreover, the interpretation of their magnetic and transport properties is made difficult by the presence of thallium or bismuth within the rocksalt layers. Thus the study of less complex compounds involving only two cations is of prime importance to understand the mechanisms which govern the physical properties of these compounds. On this basis, we have revisited the system Ca-Co-O, previously studied in air, and for which two compounds $Ca_3Co_2O_6$ and $Ca_3Co_4O_9$ were synthesized.[14,15] Only the crystal structure of the former is known to date.[16] In the present paper, we demonstrate that $Ca_3Co_4O_9$ is a misfit-layered oxide and we show that this compound exhibits MR properties below 50 K. Moreover, the single-crystal investigation of this oxide evidences the anisotropic character of the magnetoresistance which mainly appears in the $[CoO_2]_\infty$ layers. Finally, the magnetotransport properties of this compound are interpreted in two terms of superexchange and double exchange between Co^{3+} and Co^{4+} species in the $[CoO_2]_\infty$ layers, taking into account the x-ray appearance near-edge structure (XANES) observations which show a partial disproportionation of Co^{3+} into Co^{4+} and Co^{2+}.

II. EXPERIMENT

Polycrystalline $Ca_3Co_4O_9$ was prepared by heating a stoichiometric mixture of CaO and Co_3O_4 in air at 900 °C for 24 h and quenching to room temperature. Single crystals were grown from a mixture of K_2CO_3 and $Ca_3Co_4O_9$ in the mass ratio 1/7. The mixture was heated up to 880 °C in 6 h, maintained at this temperature for 50 h, and then slowly cooled. Two different kinds of crystals were obtained, needle-shaped crystals, identified as $Ca_3Co_2O_6$,[17] and very thin micalike platelets, identified as $Ca_3Co_4O_9$.

X-ray powder diffraction (XRPD) data were collected by step scanning over an angular range $5 \leqslant 2\Theta \leqslant 100°$ using a Philips vertical diffractometer equipped with a secondary graphite monochromator and working with the Cu $K\alpha$ radiation. In spite of the micalike character of the single crystals, the powder did not seem to exhibit preferred orientation phenomena. However, to minimize such possible phenomena, powder was carefully deposited on grease for x-ray data collection. Diffraction patterns were treated with the profile analysis program FULLPROF (Ref. 18) for lattice constant refinement and structure calculation.

Samples for electron microscopy were prepared by dispersing the crystallites in alcohol. The particles were deposited on a holey carbon film supported by a Cu grid. The electron diffraction (ED) study was carried out using a JEOL 200 CX microscope fitted with an eucentric goniometer ($\pm 60°$) and the high-resolution electron microscopy (HREM) with a TOPCON 002B microscope operating at 200 kV (point resolution of 1.8 Å). Both microscopes are equipped with KEVEX energy-dispersive spectroscopy (EDS) analyzers. HREM image simulations were calculated with the Mac-Tempas multislice program.

Oxygen content was determined by two methods: classical redox titration and reduction in a $Ar/H_2 = 9/1$ atmosphere at 1000 °C.

The magnetic properties were measured on single crystals with a superconducting quantum interference device (SQUID) magnetometer in the range 5–300 K. Due to their small size, the crystals were directly fixed on straws using very small quantity of grease. Their orientation were chosen so that the applied magnetic field be in the plane or orthogonally to it. Due to the small values of the paramagnetic moments of the crystals at room temperature, the high-temperature inverse susceptibility was measured on a polycrystalline ceramic sample, using a Faraday balance in 0.3 T, up to 700 K, in order to complete the curves at high temperature.

The resistivity of the crystal was measured with a four-probe technique, previously used for the study of high-T_c superconductors single crystals.[19] Electrical contacts were made of ultrasonic deposited indium. For the in-plane geometry, two indium contacts were put on the two opposite lateral sides to provide an homogeneous current injection in all the thickness (typically 20–30 μm) of the crystals and two voltage contacts were soldered on the top surface. In the transverse resistivity measurements, two pairs of contacts were deposited, each of them on the largest faces of the crystals, the current being injected across the thickness of the crystal (cross configuration). For each configuration, two crystals have been tested. Similarly to the magnetic measurements, the high-temperature resistivity (300–600 K) has been also measured on a ceramic bar of the same phase with a four-spring contact method since it was not possible to heat the indium contacts at such high temperatures.

The thermopower measurements have been performed on small and thin crystals extracted from the same batch. The setup description has already been reported elsewhere.[20]

The x-ray absorption study of these phases was performed systematically on the samples previously studied for their transport and magnetic properties. The x-ray absorption spectra at Co *K* edges were recorded at room temperature in a classical transmission mode at the EXAFS I station (channel-cut monochromator) using the synchrotron radiation of the DCI storage ring of LURE (Orsay, France) working at 1.85 GeV with a 250 mA current. The energy resolution at Co *K* edge is estimated to 1.3 eV, whereas the reproducibility of the monochromator position is as high as 0.3 eV. The normalization procedure used throughout this work was a standard one: after substraction of the same pre-edge background on the XANES and extended x-ray absorption fine structure (EXAFS) spectra, recorded in the same experimental conditions except the energy step, a point located at an energy of 800 eV from the edge, where no more EXAFS oscillations were still observable, was set to unity. Then the intensity of a point with an energy between 50 and 100 eV from the edge was recorded on the EXAFS spectrum. A point at the same energy was then localized in the XANES spectrum and its intensity set to the value recorded on the EXAFS. All the x-ray absorption spectroscopy (XAS) data presented in this paper were obtained from powder samples whose average grain size was determined by electron microscopy observations to be around 5 μm, much smaller than the absorption length estimated at the Co *K* edge for these compounds.

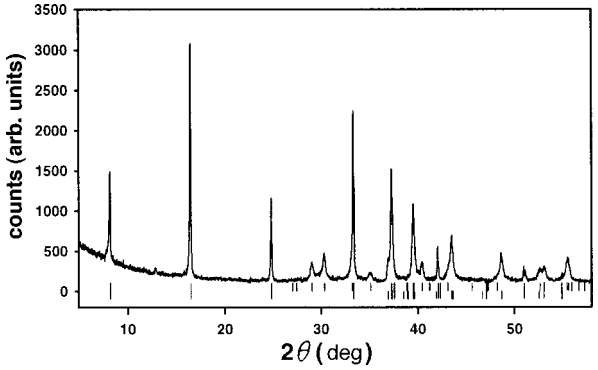

FIG. 1. Powder x-ray diffraction pattern registered with Cu $K\alpha$ radiation ($2\theta \leqslant 58°$). The vertical bars are the Bragg angle positions for S_1 (upper) and S_2 (lower) subsystems.

III. RESULTS AND DISCUSSION

A. Structural study

The x-ray powder diffraction pattern of the as-synthesized black polycrystalline sample (Fig. 1) agrees with the data previously published for $Ca_3Co_4O_9$.[14] The EDS analyses performed on numerous crystallites ''$Ca_3Co_{3.85}$'' show a slight cobalt deficiency with regard to the nominal composition, but remain close to it. It should be noticed that all the analyzed crystallites show homogeneous compositions since the cobalt content never wanders from more than 0.02 with regard to the average value. The oxygen analysis using both thermal reduction and redox titration leads to very similar results, i.e., ''$O_{9.07}$'' and ''$O_{9.02}$,'' respectively, considering four Co atoms per formula unit.

An evident lamellar habitus of the crystallites is observed by electron microscopy. The reconstruction of the reciprocal space from ED patterns [Figs. 2(a) and 2(b)] shows that the new phase is a composite structure. It is characterized by the coexistence of two monoclinic subsystems, with $[100]^*$ and $[001]^*$ as common axes and a parameter misfit along $[010]^*$. The intense reflections are indexed in two subsystems which exhibit common *a*, *c*, and β parameters and only differ by the *b* axes which are denoted by the suffixes 1 and 2:

$$S_1\{a, b_1, c, \beta\} \quad \text{with} \quad a \approx 4.8 \text{ Å}, \quad b_1 \approx 4.5 \text{ Å},$$

$$c \approx 10.8 \text{ Å}, \quad \beta \approx 98°,$$

$$S_2\{a, b_2, c, \beta\} \quad \text{with} \quad a \approx 4.8 \text{ Å}, \quad b_2 \approx 2.8 \text{ Å},$$

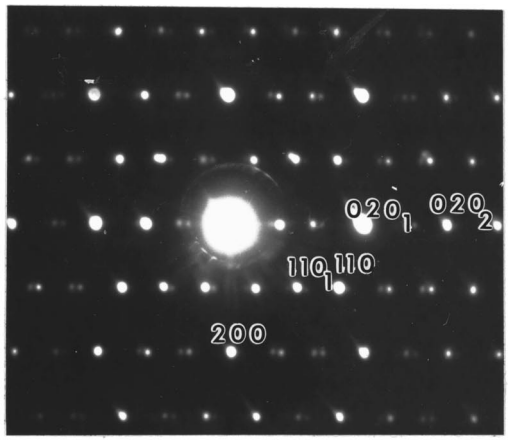

(a)

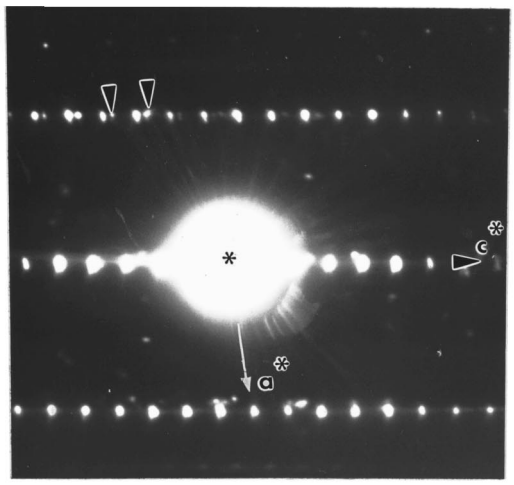

(b)

FIG. 2. (a) [001] and (b) [010] ED pattern (small arrows indicate a second system of reflections due to twinning phenomena).

$$c \approx 10.8 \text{ Å}, \quad \beta \approx 98°.$$

The XRPD pattern is then indexed (Table I) with the following parameters:

$$a = 4.8376(7) \text{ Å}, \quad b_1 = 4.5565(6) \text{ Å},$$

$$c_1 = 10.833(1) \text{ Å}, \quad \beta = 98.06(1), \quad b_2 = 2.8189(4) \text{ Å}.$$

The two subsystems of reflections are clearly observed in the [001] ED patterns [Fig. 2(a)]. In the [010] patterns, the hexagonal subsystem is scarcely visible. Such patterns exhibit great similarities with those previously reported for other composites oxides, $Tl_\alpha[(Ca,Sr)_{1-\beta}(O)]_{1+x}[CoO_2]$ and $Bi_\alpha(A_{0.75}Bi_{0.25}O)_{(3+3x)/2}CoO_2$ (A=Ca,Sr).[1–3] The a and b_1 parameters are indeed correlated to the "a_{RS}" parameter of the rocksalt (RS) structure ($a \approx b_1 \approx a_{RS}$). However, the a/b_1 ratio is significantly different from 1, expected for an ideal cubic RS subcell and suggests that the RS-related component of the misfit-layered structure is strongly distorted. The a and b_2 parameters are correlated to the "a_H" parameter of the hexagonal (H) structure of CdI_2 type ($a \approx a_H\sqrt{3}$, $b_2 \approx a_H$). The hexagonal component of the misfit layered oxides is one octahedral slice $[CoO_2]$, also observed in the A_xCoO_2 oxides with A=Na, Ca, ...[21,22] The conditions limiting the intense reflections hk_20 ($h+k_2=2n$), for the S_2 subsystem, are similar to those observed for the thallium and bismuth misfit-layered cobaltite. It is consistent with orthorhombic distortion of an hexagonal subcell. The conditions on the intense reflections hk_10 ($h+k_1=2n$) are similar to those observed for the Tl misfit oxides.

Our previous works on the misfit layered oxides[1–5] showed that the nature of the layers stacked along the c axis strongly depends on the cation composition and also of the thermal process, due to the possible mixed valence of the transition cations. In order to understand this point, the $Ca_3Co_4O_9$ oxide was investigated by high-resolution electron microscopy. The contrast was interpreted by comparing the [001] and $[hk0]$ images with those recorded for other misfit layered oxides,[1–3,5] but also sulphides.[23]

The structure was firstly explored along $[hk0]$ in order to identify the different (001) layers. Viewing the crystals along [100], a classical contrast [Figs. 3(a) and 3(b)] is obtained. For a focus value close to -55 nm[3], the heavy electron density zones appear as bright spots [Fig. 3(a)]. Three parallel rows of bright spots, forming rectangles, spaced by ≈2.3 Å are observed. In between these groups of three rows of bright dots is a row of weak and rather diffuse white dots. The three rows of very bright dots are correlated to three $[AO]_\infty$ layers of a double RS-type slice and the row of weak spots to the Co layer of the hexagonal slice. For a focus value of 25 nm [Scherzer value, in Fig. 3(b)], they appear as the darker zones and are in agreement with the above structural hypothesis.

All the $[hk0]$ images show a high regularity of the layer stacking mode along the c axis. None intergrowth defect was detected. At this point of the investigations, a first rough structural model can be proposed for this misfit-layered calcium cobaltite. It consists in the stacking of the following layers

(i) A triple $[AO]_\infty$ layer with A=Ca and Co, i.e., one double RS layer, generate the first sub system of reflections S_1. The corresponding lattice is strongly distorted with regard to the ideal cubic RS structure. They correspond to the triple rows of heavy electron density in the HREM images

(ii) A single hexagonal $[CoO_2]_\infty$ layer, observed in the A_xCoO_2 polytypes and in the other misfit oxides. It is commonly named CdI_2-type layers, but is in fact a $(111)_{RS}$ rocksalt-type layer. These layers generate the second subsystem S_2. They are on the nodes of a two-dimensional (2D) network with a pseudohexagonal symmetry ($a \approx b_2\sqrt{3}$). They correspond to the single rows of light electron density in the HREM images.

It is of course utopian to solve such a complex structure from x-ray powder data, but unfortunately, at the present time, the quality of the single crystals was too poor to allow a structural study. In order to calculate simulated HREM images, we used powder data. A commensurate supercell was considered in a first approximation, taking into consideration the fact that the ratio $b_1/b_2=1.613$ is close to 13/8 (1.625), leading to the parameters $a=4.8376$ Å, $b \approx 8b_1 \approx 13b_2 = 36.479$ Å, $c=10.833$ Å, and $\beta=98.06°$. According to the stacking sequence deduced from the $[hk0]$ images, such a supercell implies the ideal composition $Ca_{32}Co_{42}O_{100}$: 26 CoO_2 motifs for the single $[CoO_2]_\infty$

TABLE I. Powder x-ray diffraction pattern of $Ca_3Co_4O_9$ (Cu $K\alpha$ radiation) with indices for the two subsystems: $a=4.8376(7)$ Å, $b1=4.5565(6)$ Å, $c=10.833(1)$ Å, $\beta=98.06(1)$, and $b2=2.8189(4)$ Å.

$2\theta_{exp}$ (deg)	Int.	h_1	k_1	l_1	$2\theta_{cal}$ (deg)	h_2	k_2	l_2	$2\theta_{cal}$ (deg)
8.24	51	*0*	*0*	*1*	8.24	*0*	*0*	*1*	8.24
16.52	100	*0*	*0*	*2*	16.52	*0*	*0*	*2*	16.52
24.88	38	*0*	*0*	*3*	24.89	*0*	*0*	*3*	24.89
29.10	25	*1*	*1*	*1*	29.03				
30.35	339	*1*	*1*	*−2*	30.36				
33.17	10	*1*	*1*	*2*	33.19				
33.39	83	*0*	*0*	*4*	33.39	*0*	*0*	*4*	33.39
35.11	8	*1*	*1*	*−3*	35.14				
36.98	11					*1*	*1*	*0*	36.97
37.33	91	*2*	*0*	*−1*	37.28	*2*	*0*	*−1*	37.28
						1	*1*	*−1*	37.33
39.57	80	*0*	*2*	*0*	39.52	*1*	*1*	*−2*	39.59
40.45	19	*0*	*2*	*1*	40.44				
42.10	18	*0*	*0*	*5*	42.09	*0*	*0*	*5*	42.09
43.16	10	*0*	*2*	2	43.11				
43.51	46	*2*	*0*	*2*	43.45	*2*	*0*	*2*	43.45
						1	*1*	−3	43.49
48.32	2	*1*	*1*	*−5*	48.27				
48.68	35	*2*	*0*	*3*	48.59	*2*	*0*	*3*	48.59
						1	*1*	*−4*	48.71
51.07	13	*0*	*0*	*6*	51.05	*0*	*0*	*6*	51.05
52.67	17	*0*	*2*	*4*	52.67				
53.14	20	*2*	*0*	*−5*	53.13	*2*	*0*	*−5*	53.13
55.00	5					*1*	*1*	*−5*	55.01
55.59	40	*2*	*2*	*0*	55.63				
59.28	13	*2*	*2*	−3	59.30				
61.29	6	*1*	*1*	6	61.25				
62.01	7	*2*	*0*	*5*	61.94	*2*	*0*	*5*	61.94
63.64	7	*3*	*1*	−3	63.72				
64.40	6	*2*	*2*	*3*	64.36				
		1	*1*	*−7*	64.47				
65.37	2	*1*	*3*	*1*	65.35				
66.22	6					*0*	*2*	*0*	66.26
66.86	24					*0*	*2*	*1*	66.90
67.51	23					*3*	*1*	−2	67.50
68.79	7					*0*	*2*	*2*	68.81
69.39	9					*3*	*1*	−3	69.47
70.10	12	*1*	*1*	*7*	70.10				
		0	*0*	*8*	70.13	*0*	*0*	*8*	70.13

layer and 16 Ca_2CoO_3 motifs for the triple $[AO]_\infty$ layers assuming the succession ''CaO-CaO-CaO'' (Fig. 4). The ideal formula is intermediate between $Ca_{30}Co_{40}O_{90}$ (10 $Ca_3Co_4O_9$ units per supercell) and $Ca_{33}Co_{44}O_{99}$ (11 $11Ca_3Co_4O_9$ units), except for oxygen stoichiometry, and it assumes no cation vacancy. The calculated density on the basis of the ideal composition, equal to 4.68 $g\,cm^{-3}$, is slightly greater than the experimental one, measured by picnometry in carbon tetrachloride (4.47 $g\,cm^{-3}$). This result and the EDS analyses which detect a small cobalt deficiency with regard to composition ''Ca_3Co_4'' suggest that a cation nonstoichiometry cannot be excluded.

In order to move freely the triple $[AO]_\infty$ layer with regard to the $[CoO_2]_\infty$ layer, the $P1$ space group which involves 174 independent atoms in the supercell was used. Nevertheless, considering the ideal composition, fixing the coordinates of the atoms in the $[CoO_2]_\infty$ layer, and forcing those of the RS layers to vary with the magnitude, a R_{Bragg} factor of 20% was obtained.

HREM images were then calculated for the corresponding atomic coordinates, varying the focus values and crystal thickness. The [100] images [Fig. 3(c)] calculated for a crystal thickness of 25 Å exhibit an average contrast which is in agreement with the experimental images. These calculations fit with the proposed stacking mode of the layers and show that the cobaltite can be described as a misfit layered oxide with the formula $[Co_{0.5}CaO_{1.5-x}]_2[CoO_2]_{1.62}$. However, the detailed images show modulation of the contrast which is not

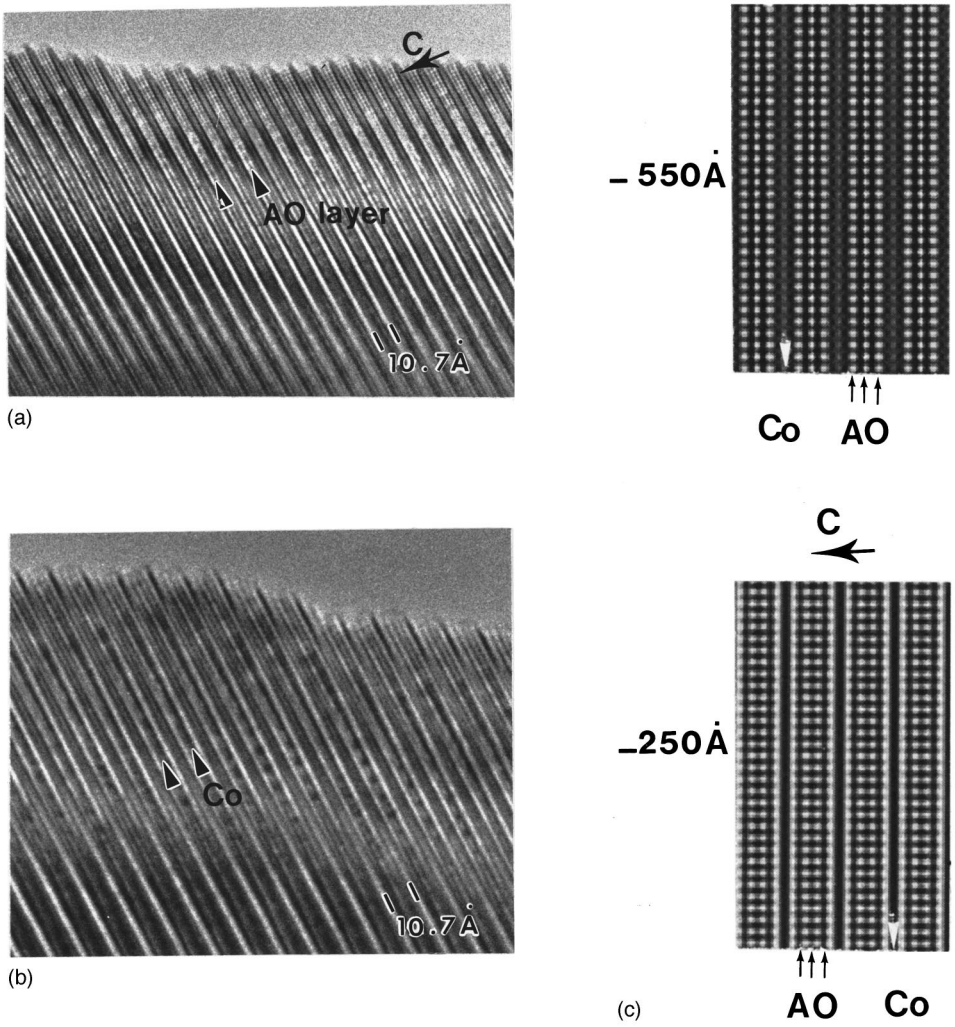

FIG. 3. [100] HREM images recorded for focus values close to (a) −550 Å, (b) −250 Å; (c) corresponding [100] theoretical images calculated for an ideal model.

simulated. This is illustrated for two experimental images selected from the through focus series and the corresponding calculated images (Fig. 3). A contrast variation is observed, which strongly affects the three adjacent $[AO]_\infty$ layers, especially the intermediate one.

The $[001]_{1,2}$ HREM images evidence two characteristics, which clearly appear depending on the focus value.

(i) An array of white spots, spaced by 2.3 Å [Fig. 5(a)]; this contrast is the signature of the RS layer, the *H* layer being scarcely visible, as usually observed in the misfit oxides and sulphides.

(ii) A strong modulation of this contrast [Fig. 5(b)] with sequences of brighter and less bright dots, which is the signature of the misfit character. In the present image, the main feature exhibits an average periodicity of 36.5 Å along *b*, which is consistent with the parameter of the supercell. It is generated by the existence of three rows running along [100] of anomalous contrast; the dots are darker in Fig. 5(a) and brighter in Fig. 5(b). Considering the contrast of the RS subsystem, the contrast is modified in one row out of three. The rows are therefore about 6.8 Å spaced, and the bright dots are in staggered positions in these rows of special contrast. The periodicity of 36.5 Å is not perfectly respected throughout the whole crystals; it locally varies along the *b* axis, which is consistent with the incommensurate character of the modulation, but moreover the highlighted rows are shifted along the second direction.

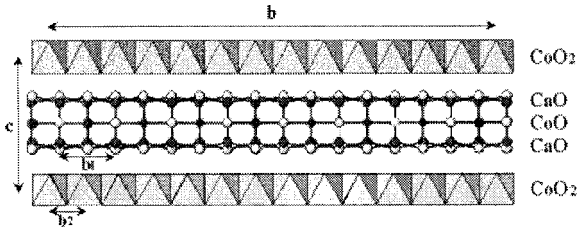

FIG. 4. Proposed structural model for ''$Ca_3Co_4O_9$'' involving a supercell with $b \sim 8b_1 \sim 13b_2$.

At this step of the work, it is straightforward that any of the aforementioned theoretical models is able to reproduce such contrast variations in the [001] calculated images, as well along [100] as along [001] [Fig. 3(c)]. This can be easily understood since only translations of a perfect RS system of three $[AO]_\infty$ layers were taken into account, but no distortions.

From the analysis of the experimental contrast, the contrast variation could be generated by nonstoichiometry phenomena at the level of the RS layers and/or strong atomic displacements, correlated to the presence of possible atom vacancies or to the mismatch between the two subsystems.

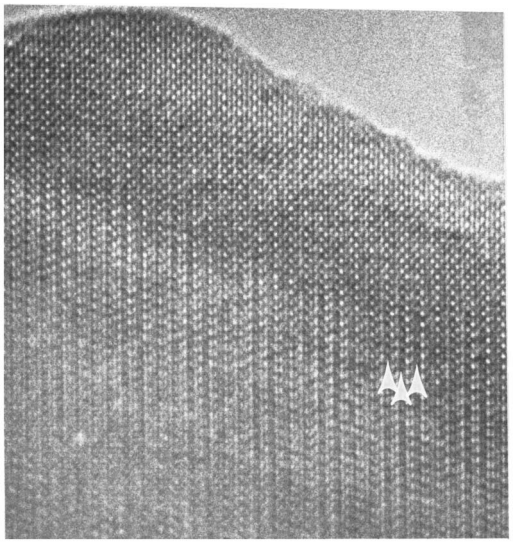

(a)

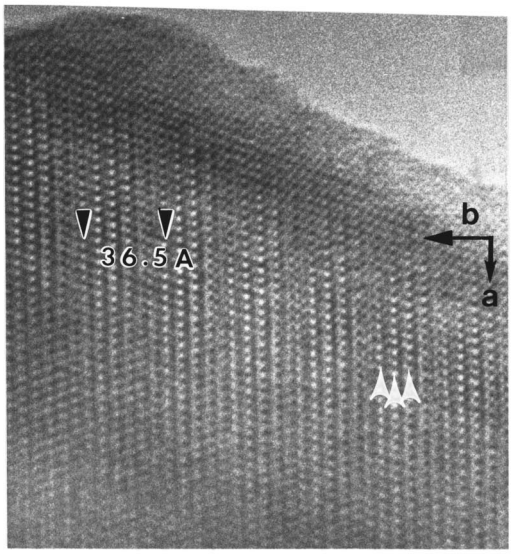

(b)

FIG. 5. [001] HREM images recorded for focus values close to (a) −550 Å, (b) −250 Å.

Due to the number of parameters, it is impossible to get accurate atomic positions. Note, however, that image calculations carried out with cationic deficiency [Fig. 6(a)] generate contrast variations which are consistent with the experimental images. Two examples are given in Fig. 6(b) for a focus value close to −550 Å; they have to be compared to Fig. 5(b) and 3(a), respectively.

The presence of cobalt in two different types of layers implies two different sets of bond distances, 1.8–1.9 Å in the $[CoO_2]_\infty$ layer, 2.2–2.4 Å in the $[AO]_\infty$ layers, and can be related to the presence of different oxidation states- +2, +3, and +4, with a mean value close to +3, to agree with the oxygen content analysis and the number of Co in each layer. To verify this hypothesis the cobaltite was studied by x-ray absorption techniques.

B. XANES spectroscopy

The cobalt *K* absorption edges of the $Ca_3Co_4O_9$ compound is shown in Fig. 7 as well as the ones of La_2CoO_4 and

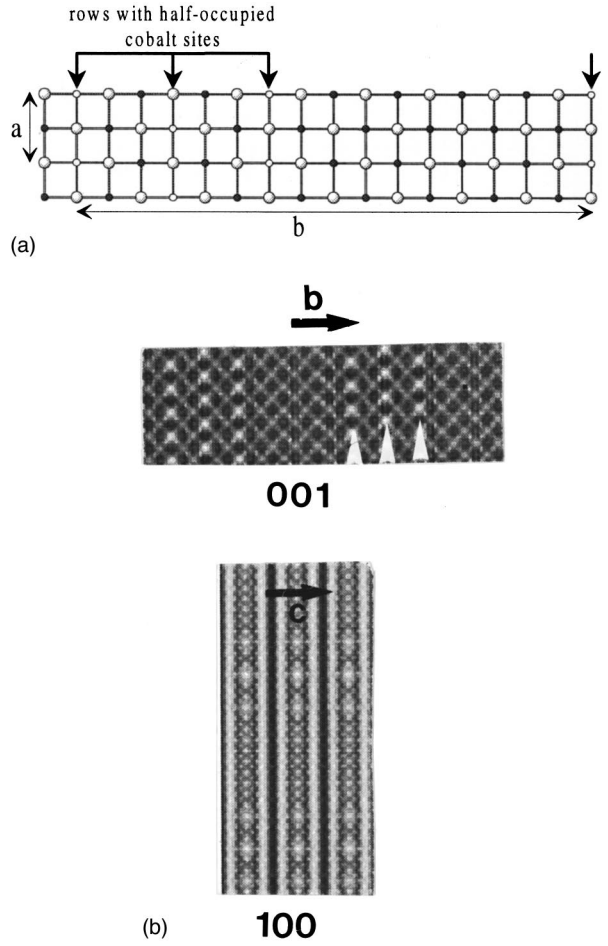

FIG. 6. (a) Possible structural model, assuming cobalt vacancies, used for HREM image calculations. Fully occupied cobalt sites are drawn as small solid circles and half-filled cobalt sites are drawn as small open circles. (b) Calculated images of the [001] and [100] series: focus value −550 Å, crystal thickness 36 Å.

$LaCoO_3$, used as reference for Co(II) and Co(III) formal charges in octahedral coordination, respectively.

Both reference compounds La_2CoO_4 and $LaCoO_3$ exhibit well-known atomic structures and Co-O distances. La_2CoO_4

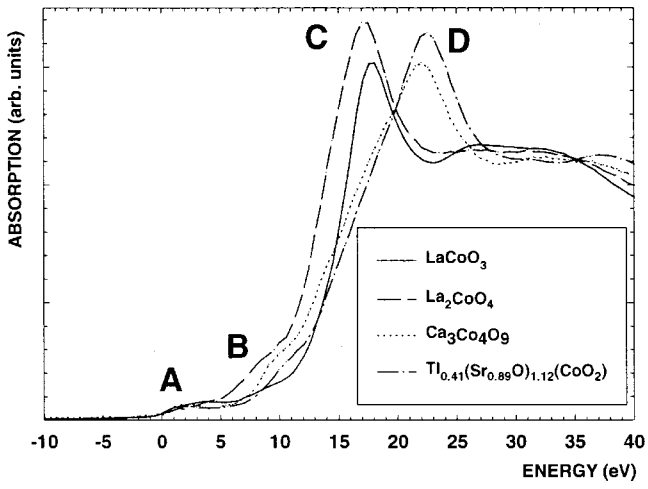

FIG. 7. Normalized Co *K* edges at room temperature for some cobalt oxide references, ''$Ca_3Co_4O_9$'' and $Tl_{0.41}(Sr_{0.89}O)_{1.12}(CoO_2)$.

crystallizes in the K_2NiF_4-type structure in which the Co octahedra are tetragonally distorted with four short Co-O distances at 1.94 Å and two long Co-O distances along the *c* axis at 2.03 Å. Conversely $LaCoO_3$ presents a small othorhombic distortion of the perovskite structure with six Co-O distances close to 1.92 Å.

A fourth edge is shown (Fig. 7) corresponding also to a misfit compound studied earlier, $Tl_{0.41}(Sr_{0.89}O)_{1.12}(CoO_2)$,[1] with a structure closely correlated to that of the $Ca_3Co_4O_9$ compound. The Co *K* edge of the Tl misfit published earlier, using a previous study at the Co *K* edge of some Co(II) and Co(III) oxides in various Co environments,[2] was analyzed through the existence of a mixed valence state in the $[CoO_2]$ layers with an estimated formal charge for Co around +3.4. Such a result was deduced not only from the shift of the edge towards high energy with respect to $LaCoO_3$ but also from peak *C* energy (22 eV) which corresponds to short Co-O distances. The XANES features at the Co *K* edge correspond to electronic transitions from the $1s$ core level to (a) molecular orbitals built from hybridization of Co($4p$)-O($2p$)-Co($3d$) orbitals in the prepeak area (*A* in Fig. 7) and (b) the main Co($4p$) empty levels hybridized with O($2p$) and split by the crystal field in the main absorption jump area (*B*, *C*, and *D* in Fig. 7).

The $Ca_3Co_4O_9$ spectrum is quite similar in shape and width to the Tl misfit one, but it exhibits two main differences.

(i) The midpoint of the main absorption jump is located at the same energy as the one of $LaCoO_3$, a result indicating that the average formal charge of Co inside the $Ca_3Co_4O_9$ misfit compound is close to +3.

(ii) At low energy, in the 6–14 eV range, there is a spectral density much larger for $Ca_3Co_4O_9$ than for $LaCoO_3$; especially, a shoulder can be observed at 9.5 eV in a way similar to what is observed on the La_2CoO_4 spectrum reference for an octahedral Co^{2+} formal charge.

It has been shown earlier by Natoli[24] that the peak energies on a XANES spectrum can be linked empirically to the *M*-O distances through the simple relationship

$$(E-E_0)R^2=K,$$

which holds for transition metal compounds at *K* edges and where *E* and *R* are the peak energy and corresponding *M*-O distance, whereas E_0 and *K* are constants to be determined for a given edge. To apply the so-called Natoli's rule to the Co *K* edge, one needs to determine the E_0 and *K* contants through precise knowledge of the Co-O distances in the two reference oxides La_2CoO_4 and $LaCoO_3$. The energies of *C* peaks were determined in Fig. 7, and the results are shown in Table II. The Co-O distances corresponding to the *B* and *D* peaks of our misfit compound are also given in Table II.

The long Co-O distances ($R_{Co\text{-}O}=2.25$ Å) are in agreement with Co-O distances expected in the rocksalt-type layers of the $Ca_3Co_4O_9$ compound. They sign the probable existence of Co^{2+} formal charge inside these layers.

The *D* peaks of $Ca_3Co_4O_9$ and $Tl_{0.41}(Sr_{0.89}O)_{1.12}(CoO_2)$ misfit compounds at high energies correspond to Co-O distances ($R_{Co\text{-}O}\approx 1.8$ Å; see Table II) which may be associated with the short ones expected in the $[CoO_2]_\infty$ layers. Although no pure Co^{4+} oxide could be found as reference, these short Co-O distances were associated previously with the presence of Co^{4+} formal charge in the Tl misfit compound. But taking into account the Co^{3+} average formal charge and the presence of Co^{2+} inside the rocksalt-type layers, one is led to the conclusion that Co should exhibit a mixed formal charge in the $[CoO_2]_\infty$ layers, between +3 and +4.

TABLE II. Application of the Natoli's rule for the calculation of Co-O distances in $Ca_3Co_4O_9$ using $E_0=-12.71$ eV and $K=112.52$ eV Å^2 (calculated from the references).

Compounds	Energy (eV)	*R* (Å)	Coordination
La_2CoO_4 (reference)	17.2	1.94	6
$LaCoO_3$ (reference)	17.8	1.92	6
$Ca_3Co_4O_9$	9.5	2.25	6
$Ca_3Co_4O_9$	22	1.80	6

A limit model can be thus proposed assuming the ideal cationic composition and 3+ as average oxydation state for cobalt:

$$[Co_{10}^{3+}Co_{16}^{4+}O_{52}][Ca_{32}^{2+}Co_{16}^{2+}O_{43}].$$

C. Magnetic properties

The electron configuration of Co^{3+} ions is $3d^6$, but with respect to the closeness of the crystal-field splitting ($10Dq$) between t_{2g} and e_g states and the Hund coupling energy (exchange energy), the spin state configuration of high spin (HS), $t_{2g}^4e_g^2$, $S=2$, and low spin (LS), $t_{2g}^6e_g^0$, $S=0$, are very close in energy. This was shown for $LaCoO_3$, which exhibits two spin-state transition as the temperature increases, from LS to intermediate spin (IS, $t_{2g}^5e_g^0$, $S=1$), and then from IS to HS.[25]

The energetically more favorable high-spin state $S=5/2$ for Co^{4+} ($t_{2g}^3e_g^2$) was confirmed by x-ray photoemission spectroscopy (XPS).[26] However, the mixed valency $Co^{(III)3+}/Co^{(IV)4+}$ assumed in the CoO_2 planes of $Ca_3Co_4O_9$ makes it very difficult to presume the ground spin state. The magnetic susceptibility (χ) as a function of temperature has thus been collected in order to extract the effective magnetic moment per Co. However, the measurements performed with single crystals in the $H\|(ab)$ and $H\|c$ geometries for 5 K $<T<$ 300 K yield too low magnetic moment values, but linear $\chi^{-1}(T)$ curves seem to be obtained for the highest temperatures (Fig. 8). According to the low measured values for single crystals, $Ca_3Co_4O_9$ ceramics have been used to measure the susceptibility by using a Faraday balance. The corresponding $\chi^{-1}(T)$ curve (Fig. 9) shows an abrupt change around 420 K, beyond which a Curie-Weiss law $\chi=\chi_0+C/(T-\theta p)$ can be applied. Above 420 K, a value $\mu_{eff}=2.8\mu_B$/mol of Co is calculated, whereas for $T<400$ K this value is reduced to $1.3\mu_B$/mol of Co. The abrupt change occurring at 420 K may correspond to a spin-state transition of cobalt. For the low-temperature range ($T<400$ K), by considering the ''ideal'' formula $[Co_{10}^{3+}Co_{16}^{4+}O_{52}][Ca_{32}^{2+}Co_{16}^{2+}O_{43}]$, the $1.3\mu_B$ value is compatible with the LS configuration of the whole Co cations, di-, tri-, and tetravalent, which yield the theoretical value $\mu_{eff}=1.44\mu_B$. On the

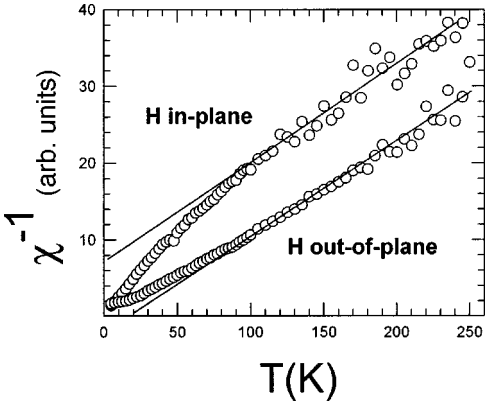

FIG. 8. Temperature dependence of inverse of the magnetic susceptibility registred for a single crystal with H parallel and perpendicular to the CoO_2 planes ($\mu_0 H = 0.3$ T).

other hand, for $T > 420$ K, the experimental value ($2.8\,\mu_B$) could be explained by an IS configuration for Co^{4+} and Co^{3+} and LS for Co(II), which leads to $\mu_{\text{eff}} = 2.83\mu_B$. The magnetic transition could then be viewed as a spin-state transition from LS to IS for Co^{4+} and Co^{3+}. It should be emphasized that the magnetic transition goes with an anomaly at the same temperature on the resistivity curve of the polycrystalline sample which is enlarged in the inset of Fig. 10. This electronic transition indicates a change from a metallic behavior below 410 K to an activated behavior above this temperature. It should also be emphasized that the Co(III) and Co(IV) LS states at low temperature for the cobalt species in the $[CoO_2]_\infty$ planes are in good agreement with the spin states reported for trivalent and tetravalent cobalt in the metallic bronze-type $NaCo_2O_4$,[27] which exhibits similar cobalt oxygen planes. It should be pointed out that the Co-O-Co bond angle in these CoO_2 layers is close to 90°, in contrast with that encountered in the widely studied cubic perovskites.

D. Transport properties

The two-dimensional nature of the transport properties is evidenced in Fig. 11, where the in-plane (ρ_{ab}) and out-of-plane (ρ_c) resistivities vs temperature are plotted. The $\rho_{ab}(T)$ curves show a metallicline behavior as T decreases from 300 to 50 K, whereas ρ_c is much higher and its T dependence is indicative of a semiconducting like behavior.

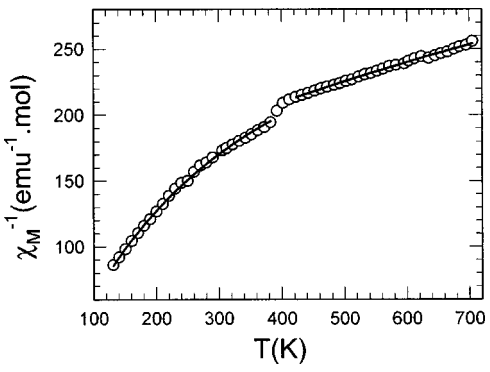

FIG. 9. Temperature dependence of the inverse molar magnetic susceptibility for a ceramic sample ($\mu_0 H = 0.3$ T).

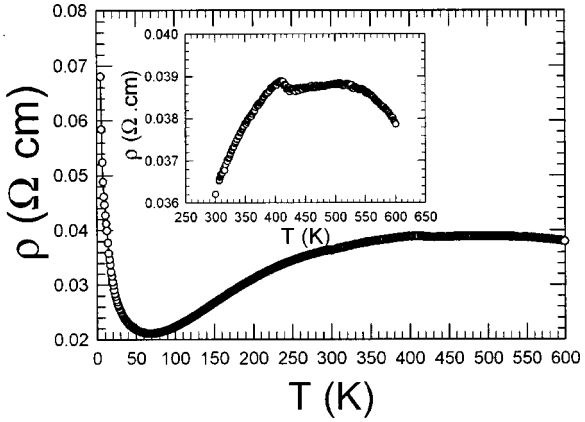

FIG. 10. Temperature dependence of the electrical resistivity (ρ) measured for a sintered bar of ''$Ca_3Co_4O_9$'' ceramic. Inset: enlargement showing the change at 400–420 K.

However, ρ_{ab} shows a reentrant behavior below 50 K, suggesting a localization effect. The $\rho_{ab}(300\,\text{K})$ values measured for three different single crystals are found to be in the range 10–40 mΩ cm. In spite of the lack of accuracy due to the difficulty to measure the thickness of the crystals, these values are much higher than that reported for the in-plane resistivity of $NaCo_2O_4$ [$\rho_{ab}(300\,\text{K}) = 2\times10^{-1}$ mΩ cm].[27]

It should be noticed that the $\rho_{ab}(T)$ measured for the single crystals (Fig. 11) and $\rho(T)$ measured on ceramics (Fig. 10) are quite similar; this shows that the ceramic resistivity is governed by ρ_{ab}, consistently with the large anisotropy ($\rho_{ab} \ll \rho_c$).

A very remarkable result concerning the transport properties of these crystals is the existence of magnetoresistance (MR). The comparison of the $\rho_{ab}(T)$ curves registered upon cooling under 0 and 7 T [Fig. 12(a)] shows that a large negative magnetoresistance reaching -35% appears in the ab plane. This MR is only observed below 50 K, and its magnitude increases as T decreases. The comparison of the ρ_c curves under 0 and 7 T [Fig. 12(b)] shows a much smaller negative MR effect, always in between 0 and 5%. The negative MR is limited to the low-temperature range where the localization occurs. We can speculate that the latter is due to the decrease of spin scattering as a consequence of applied magnetic field. The same kind of mechanism may act along the transverse direction, but its mechanism is complicated by

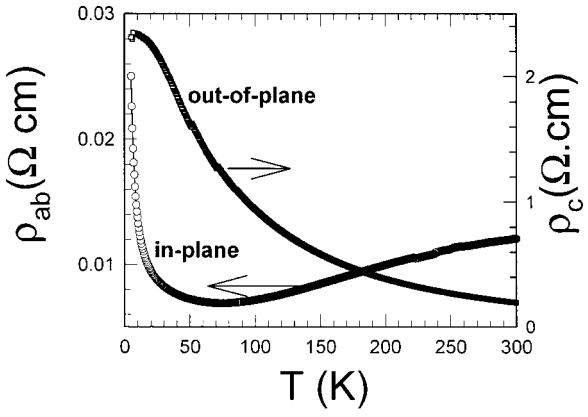

FIG. 11. In-plane [$\rho_{ab}(T)$] and out-of-plane [$\rho_c(T)$] resistivity curves.

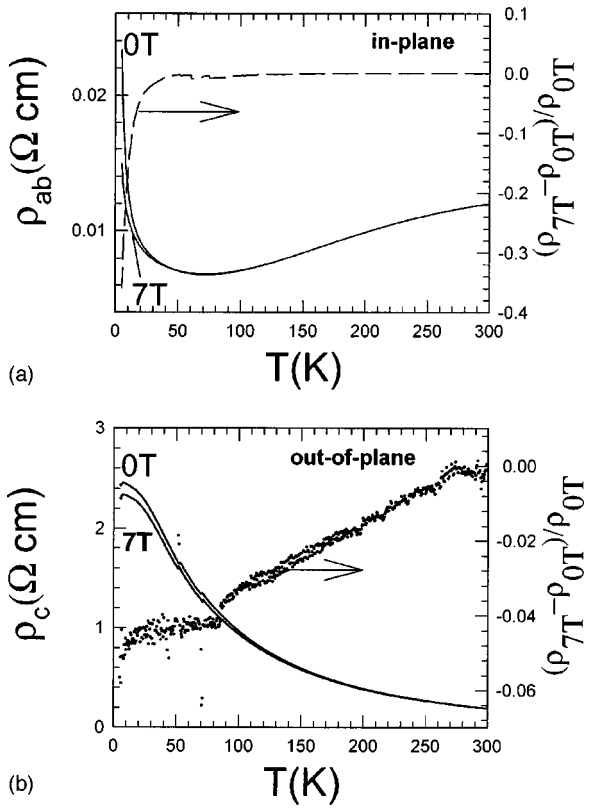

FIG. 12. $\rho(T)$ curves of a crystal registered upon cooling in and in the absence of applied magnetic field (7 and 0 T, respectively). The magnetoresistance as a function of T is also given. (a) ρ_{ab}, (b) ρ_c.

the weak interplanar coupling. The existence of MR properties in the planes containing trivalent and tetravalent cobalt is also consistant with the MR reported for 3D and 2D cobaltites containing the same species. It should be pointed out that, in the $[CoO_2]_\infty$ planes of the title oxide, the CoO_6 octahedra are not connected by their apices so that the present MR for edge-shared octahedra of Co^{3+} and Co^{4+} is found for the first time.

The temperature dependence of in-plane thermoelectric power is shown in Fig. 13. The positive value indicates that the majority of charge carriers have holelike character. Both its large magnitude of 125 $\mu V\,K^{-1}$ and weak temperature dependence below 300 K contrast with the small value and

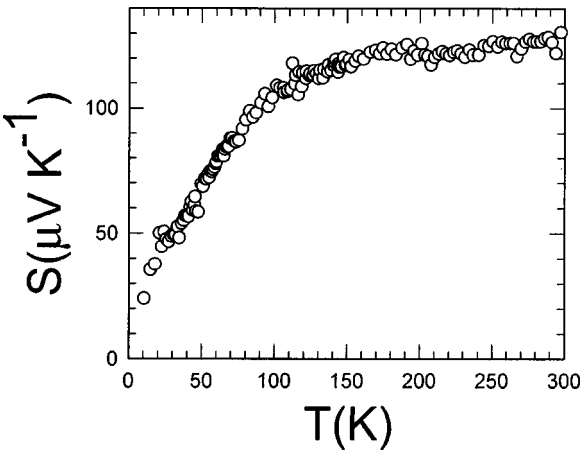

FIG. 13. Temperature dependence of the thermopower (Seebeck S) of a crystal.

metallic character of the electrical resistivity. The high and positive thermoelectric power values, observed in our single crystals, are consistent with data recently reported for ceramics[28] and for structurally related $NaCo_2O_4$ single crystals.[29] A detailed analysis of the thermoelectric power is out of the scope of this paper; in the following, we just sketch two scenarios which can elucidate the apparent discrepancy between metalliclike electrical resistivity and surprisingly high thermoelectric power. The first one deals with the energetic proximity of different ground magnetic states of cobalt discussed in the previous section. This is supported by magnetic transition observed at ~420 K and commented as a ''spin-state transition.'' Such magnetic instability introduces for relevant carriers an additional degree of freedom, which, superimposed onto normal diffusion thermoelectric power, can significantly increase its absolute value.[30] Let us note that the spin fluctuations were already proposed as possible explanation of large thermoelectric power in $NaCo_2O_4$ single crystals and $Na_{1.1-x}Ca_xCo_2O_4$ polycrystalline solid solutions.[29,31] Another tentative explanation of unusually large positive thermoelectric power is based on the existence of holelike carriers located on ''oxygen atoms'' and moving in nonmagnetic or magnetically feeble background of Co^{III} and Co^{IV} ions. The relevance of such hypothesis is justified by the very short distance between cobalt and oxygen atoms in CoO_2 layers when the energetic proximity of Co $3d$ and O $2p$ states can result in partial electron transfer from oxygen to cobalt as pointed out in, e.g., $SrCoO_3$.[32]

*Corresponding author: FAX: 33 2 31 95 16 00. Email address: claude.michel@ismra.fr

[1] Ph. Boullay, B. Domenges, M. Hervieu, D. Groult, and B. Raveau, Chem. Mater. **8**, 1482 (1996).
[2] Ph. Boullay, R. Seshadri, F. Studer, M. Hervieu, D. Groult, and B. Raveau, Chem. Mater. **10**, 92 (1998).
[3] M. Hervieu, Ph. Boullay, C. Michel, A. Maignan, and B. Raveau, J. Solid State Chem. **142**, 305 (1999).
[4] H. Leligny, D. Grebille, O. Perez, A. C. Masset, M. Hervieu, C. Michel, and B. Raveau, C. R. Acad. Sci., Paris, IIc **2**, 409 (1999).
[5] H. Leligny, D. Grebille, O. Perez, A. C. Masset, M. Hervieu, and B. Raveau, Acta Crystallogr., Sect. B (to be published).
[6] E. Mackovicky and B. G. Hyde, Struct. Bonding (Berlin) **46**, 11 (1981).
[7] G. A. Wieger and A. Meerschault, J. Alloys Compd. **178**, 351 (1992).
[8] J. Rouxel, C. R. Acad. Sci., Ser. IIb: Mec., Phys., Chim., Astron. **323**, 41 (1996).
[9] S. Yamaguchi, H. Taniguchi, H. Takagi, T. Arima, and Y. Tokura, J. Phys. Soc. Jpn. **54**, 1885 (1995).
[10] R. Mahendiran, A. K. Raychaudhuri, A. Chaimini, and D. D. Sarma, J. Phys.: Condens. Matter **7**, L561 (1995); R. Mahendiran and A. K. Raychaudhuri, Phys. Rev. B **54**, 16 044 (1996).
[11] G. Briceno, H. Chang, X. Sun, P. G. Schultz, and X. D. Xiang, Science **270**, 273 (1995).
[12] D. Groult, C. Martin, A. Maignan, D. Pelloquin, and B. Raveau, Solid State Commun. **105**, 583 (1998).

[13] A. Maignan, C. Martin, D. Pelloquin, N. Nguyen, and B. Raveau, J. Solid State Chem. **142**, 247 (1999).
[14] C. Brisi and P. Rolando, Ann. Chim. (Rome) **58**, 676 (1968).
[15] E. Woermann and A. Muan, J. Inorg. Nucl. Chem. **32**, 1455 (1970).
[16] H. Fjellvag, E. Guldbransen, S. Aasland, A. Olsen, and B. C. Hautback, J. Solid State Chem. **117**, 300 (1995).
[17] A. Maignan, C. Michel, A. C. Masset, C. Martin, and B. Raveau (unpublished).
[18] J. Rodriguez-Carvajal (unpublished).
[19] V. Hardy, A. Maignan, C. Martin, F. Warmont, and J. Provost, Phys. Rev. B **56**, 130 (1997).
[20] D. Sedmidubsky, E. Pollert, J. Hejtmanek, and P. Vasek, Physica C **232**, 104 (1994).
[21] R. A. McIntyre, A. U. Falster, S. Li, W. B. Simmons, Jr., C. J. O'Connor, and J. B. Wiley, J. Am. Chem. Soc. **120**, 217 (1998).
[22] L. B. Cushing and J. B. Wiley, J. Solid State Chem. **141**, 385 (1998).
[23] S. Kuypers, J. Van Landuyt, and S. Amelinckx, J. Solid State Chem. **86**, 212 (1990).
[24] N. Natoli, in *Exafs and Near Edge Structure*, edited by A. Bianconi, L. Incoccia, and S. Stipcich, Springer Series in Thermal Physics Vol. 27 (Springer, New York, 1983).
[25] S. Yamaguchi, Y. Okimoto, H. Taniguchi, and Y. Tokura, Phys. Rev. B **53**, R2926 (1996).
[26] A. Chainani, M. Mathew, and D. D. Sarma, Phys. Rev. B **46**, 9976 (1992).
[27] R. Ray, A. Ghoshray, and K. Ghoshray, Phys. Rev. B **59**, 9454 (1999).
[28] S. Li, R. Funahashi, I. Matsubara, K. Ueno, and H. Yamada, J. Mater. Chem. **9**, 1659 (1999).
[29] I. Terasaki, Y. Sasako, and K. Uchinokura, Phys. Rev. B **56**, 12 685 (1997).
[30] P. M. Chaikin and G. Beni, Phys. Rev. B **13**, 647 (1976).
[31] T. Kawata, Y. Iguchi, T. Itoh, K. Takahata, and I. Terasaki, Phys. Rev. B **60**, 10 584 (1999).
[32] S. F. Matar, A. Villesuzanne, and M. Uhl, J. Mater. Chem. **6**, 1785 (1996).